ACS APPLIED MATERIALS & INTERFACES

Research Article

www.acsami.org

Copper-Diffused $AgInS_2$ Ternary Nanocrystals in Hybrid Bulk-Heterojunction Solar Cells: Near-Infrared Active Nanophotovoltaics

Asim Guchhait and Amlan J. Pal*

Department of Solid State Physics, Indian Association for the Cultivation of Science, Jadavpur, Kolkata 700032, India

Supporting Information

ABSTRACT: We have grown copper-diffused $AgInS_2$ ternary nanocrystals in order to introduce the nanoparticles in organic/inorganic bulk-heterojunction devices for photovoltaic applications. Here, copper diffuses to vacant sites and improves conductivity of the nanocrystals. Upon use of such copper-diffused nanoparticles that led to a decrease in internal resistance of sandwiched devices based on the bulk-heterojunction, there has been a marked improvement in short-circuit current under white light illumination. Due to a red-shift in the optical absorption spectrum of the nanoparticles upon copper diffusion, the devices moreover acted as near-infrared (IR) active photovoltaic solar cells. From current−voltage characteristics and impedance spectroscopy of the devices, we optimized performance of the photovoltaic devices. To do so, we have varied the content of diffused copper in $AgInS_2$ nanoparticles and also the weight-ratio between the polymer and the nanoparticles of the hybrid bulk-heterojunction devices.

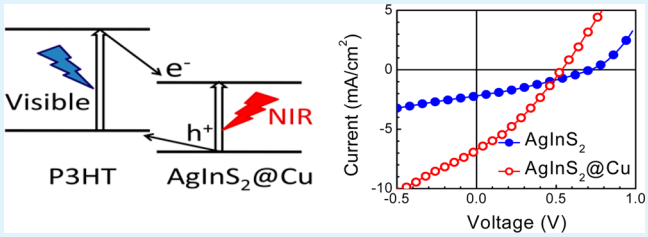

KEYWORDS: *copper-diffused $AgInS_2$ nanocrystals, hybrid bulk-heterojunction, exciton dissociation, photovoltaic devices, near-IR active solar cells*

1. INTRODUCTION

In recent years, semiconductor quantum structures are being incorporated in organic photovoltaic devices based on bulk-heterojunctions.[1−3] Advantages of nanocrystals are manifold: (i) multiple excitons are generated out of one photon thereby reducing thermalization loss, (ii) carrier mobility is higher in inorganic nanostructures as compared to that in organic semiconductors, (iii) they are stable as compared to their organic counterpart, and (iv) energy bands of nanocrystals can be tuned by varying their size, shape, dopants, etc. to suit an application.

The ability to tune energy bands of nanocrystals has a large role to play in designing a photovoltaic device.[4] In such devices that are generally composed of two materials, a staggered (type II) band alignment between the materials has to be formed so that excitons generated in either of them can become dissociated through a photoinduced electron- or hole-transfer process. In an organic/inorganic hybrid bulk-heterojunction, exciton dissociation occurs due to energy mismatch between the lowest unoccupied molecular orbital (LUMO) of the organic and the conduction band-edge of inorganic semiconductors. A mismatch between the highest occupied molecular orbital (HOMO) of the organic and the valence band-edge of an inorganic nanostructure is equally important for exciton dissociation justifying the importance of tuning of energy bands of nanocrystals.[5,6]

The quest for suitable nanomaterials can be considered to be the next generation research on organic photovoltaic devices. The choice of nanomaterials ranged from metallic to semiconducting covering gold or silver nanoparticles,[7] carbon nanostructures,[8,9] II−VI and IV−VI systems,[10,11] and so on. Doped systems did not stay behind due to the dopants' ability to tune the bandgap; copper-, nitrogen-, or manganese-doped CdS (or CdSe) nanoparticles have been used in fabricating thin-film photovoltaic devices or quantum dot sensitized solar cells (QDSSCs).[12−14] Apart from the energy of band-edges, a high extinction coefficient has been another parameter that is being considered in the search for suitable nanostructured materials to be used in photovoltaic devices.[15]

In this direction, silver-indium-disulfide ($AgInS_2$) nanoparticles have been considered for their intense absorption in the visible to near-infrared (IR) region. The ternary chalcopyrite semiconductor nanoparticles of I−III−VI_2 groups that more importantly do not contain any toxic elements are being used as heavy metal-free sensitizers for "green" QDSSCs.[16−18] Such nanoparticles, along with other inorganic nanostructures[18−20] or in a *p*-type conjugated polymer matrix,[21,22] have also been used as hybrid bulk-heterojunction solar cells.

$AgInS_2$ nanoparticles are associated with some vacancies at different constituent atom sites.[23] The vacancies led to the formation of defect states followed by a sharp decrease in crystallinity and carrier mobility. The vacancies can be improved by annealing the nanoparticles under the vapor of constituting atoms.[24] Another method to improve and control

Received: January 24, 2013
Accepted: April 26, 2013
Published: May 8, 2013

the crystallinity is through diffusion of suitable elements, such as zinc, tin, etc.

In photovoltaic devices, one aims to enhance light absorption ability and carrier mobility. Recently, kesterite and stannite type compounds, such as, $ZnS-CuInS_2-AgInS_2$ solid solutions and $(Cu_xAg_{1-x})_2ZnSnS_4$ ($0 < x < 1$), where the ratio of copper and silver elements was varied to improve the light absorption, have been used for photocatalysis applications.[25,26] In this direction, we have introduced copper-diffused $AgInS_2$ nanoparticles; copper diffusion was made possible during the nanoparticle synthesis process with an aim (1) to improve crystallinity of the nanocrystals, (2) to enhance absorbance in the visible and near-IR regions, and (3) to increase electrical conductivity and carrier mobility. Since there has been no report on using diffused/doped $AgInS_2$ nanocrystals in photovoltaic devices, we have fabricated and characterized hybrid bulk-heterojunction devices based on such nanoparticles for photovoltaic applications. The choice of copper as an element that diffuses to the nanoparticles has led to a shift in optical absorption toward the red, so that the near-IR region of solar spectrum can also be absorbed to achieve near-IR active photovoltaic devices.

2. EXPERIMENTAL SECTION

Synthesis of $AgInS_2$ Nanoparticles. For the synthesis of $AgInS_2$ nanoparticles, we followed reported procedures with some modifications.[27,28] We used silver(I) acetate (CH_3COOAg) and indium-(III) acetate ($In(CH_3COO)_3$) as silver and indium precursors, respectively. At first, we prepared a stock solution of indium by dissolving 1 mmol of indium acetate in 3.2 mL of oleic acid and 6.8 mL of 1-octadecene (ODE). A 0.1 mmol of silver acetate was dissolved in 5 mL of ODE and 1 mL of 1-dodecanethiol (DDT) in a three-neck reaction flask. The solution was degassed by purging ultrapure nitrogen for 15 min. One mL of the indium stock solution (0.1 mmol) was injected into the mixture and degassed for another 15 min. The temperature of the mixed solution was then raised to 160 °C. At this stage, 2.5 mL of a sulfur stock solution, prepared by dissolving 0.3 mmol of sulfur (in excess to that required for the reaction) in 2 mL of ODE and 0.5 mL of oleylamine, was injected to the reaction flask. The temperature of the flask was further raised to 180 °C, and reaction was allowed to continue for 30 min to complete the growth of nanocrystals. The temperature of the reaction flask was then cooled down to room temperature. The DDT-capped $AgInS_2$ nanoparticles were extracted by repeated precipitation in chloroform/ethanol followed by centrifugation at 8000 rpm. The final precipitant was dissolved in chloroform for further characterization and device fabrication.

Synthesis of Copper-Diffused $AgInS_2$ Nanoparticles ($AgInS_2$@Cu). For the synthesis of copper-diffused $AgInS_2$ nanoparticles, we prepared a copper stock solution by dissolving 2 mmol of copper chloride ($CuCl_2 2H_2O$) in 10 mL of oleylamine at 80 °C under nitrogen environment. For copper diffusion into $AgInS_2$ nanoparticles, a measured amount of copper stock solution was injected dropwise to the reaction mixture that has already been used to grow the nanoparticles for 5 min. While the initial temperature of the reaction was 160 °C, the temperature was further raised to 180 °C and aged for 20 min. During the reaction, oleylamine reduces Cu(II) to Cu(I) at the temperature of the flask before diffusion of copper to $AgInS_2$ nanocrystals took place. Particles were separated following the protocol used for $AgInS_2$ nanoparticles. Concentration of diffused copper was varied by changing the amount of the injected copper stock solution (0.05, 0.10, 0.15, and 0.20 mL) into the reaction flask. The copper-diffused nanocrystals will henceforth be denoted as $AgInS_2$@Cu(x.xx), where x.xx was the amount of copper stock solution that was injected in the reaction flask. Content of copper in the nanoparticles was estimated with atomic absorption spectroscopy.

Synthesis of $CuInS_2$ Nanoparticles. To grow $CuInS_2$ nanoparticles, we used copper(I) acetate (CH_3COOCu) and indium(III) acetate as the copper and indium precursors, respectively, and followed the reaction procedure that was used to grow $AgInS_2$ nanoparticles.

Characterization of the Nanoparticles. The nanoparticles were characterized with UV–visible-NIR optical absorption spectroscopy, transmission electron microscopy (TEM), high-resolution TEM (HR-TEM), and scanning transmission electron microscopy (STEM) images and X-ray diffraction (XRD) studies. The measurements were carried out with a Varian 5000 UV–vis-NIR spectrophotometer, JEM 2100F Jeol TEM, and Bruker D8 advanced X-ray powder diffractometer, respectively.

Device Fabrication. Devices were fabricated on glass substrates coated with indium tin oxide (ITO) strips. The ITO electrodes had a surface resistance of 15 Ω/sq. They were cleaned following a standard protocol. The entire device fabrication process was carried out inside a glovebox that was equipped with a weighing balance, a magnetic stirrer, a hot plate fitted with a temperature controller, and a spin-coating unit. At first, a 15 nm PEDOT:PSS (Baytron P 4083) layer was spun on ITO substrates at a speed of 5000 rpm. PEDOT:PSS films were annealed at 150 °C for 15 min on a hot plate. To spin a layer of the active material, P3HT polymer and the nanoparticles were mixed thoroughly in a chloroform solution with a weight ratio of 1:1 and a total concentration of 20 mg/mL. Here, P3HT represents regioregular poly(3-hexylthiophene) that had a molecular weight of 87 000 g/mol and a regioregularity of 98%. The layer of P3HT:nanoparticle blend solution was spun on PEDOT:PSS films at a speed of 2000 rpm for 60 s. While forming P3HT:nanoparticle films, we took $AgInS_2$@Cu nanoparticles with four different contents of diffused copper. In addition, we also took $AgInS_2$ and $CuInS_2$ separately in P3HT as two extremes to form the active layer. That is, we spun six types of active layers.

For another set of devices, we prepared solutions of active materials for different weight ratios between P3HT and $AgInS_2$@Cu(0.10). Here, we did not vary the content of diffused copper in the nanocrystals. The polymer to nanoparticle weight ratios were 4:1, 2:1, 1:1, and 1:2. Here also, the active layers of P3HT:$AgInS_2$@Cu(0.10) were spun on a PEDOT:PSS layer. The films were annealed at 120 °C for 20 min. Finally, a 100 nm film of aluminum (Al) as strips orthogonal to ITO electrodes was thermally evaporated under vacuum ($\sim 10^{-6}$ Torr) to complete the fabrication process of the sandwiched devices. Overlap of ITO and Al strips defined the area of the devices (4 mm^2). After aluminum evaporation, the devices were further annealed at 140 °C for 20 min under the inert environment of the glovebox.

Device Characterization. To characterize the devices for solar cell applications, the sandwiched structures were taken out of the glovebox and kept in a shielded metal chamber under vacuum. The metal chamber was fitted with a quartz window. Current–voltage (I–V) characteristics of the devices under dark and illumination conditions were recorded with a Yokogawa 7651 dc voltage source and a Keithley 6517 Electrometer that recorded the device current. The instruments were interfaced with a PC through a general-purpose interface bus (GPIB). A Newport-Stratfort 150 W Solar Simulator provided the white light illumination. For a near-IR illumination, we used an optical cast IR long pass filter (Edmund Optics) which transmitted above 650 nm. To record photoaction spectra of the devices, Jobin-Yvon H20 and H20 FIR monochromators were used for the 300–600 nm and 600–1000 nm regions, respectively.

Impedance spectroscopy of the devices was recorded with a Solartron Impedance Analyzer 1260A in the 10 Hz to 1 MHz region (8 points/decade) with 50 mV rms as a test voltage. Measurements under dark and illumination conditions were carried out with the instrument's software. The impedance analyzer was also controlled by a PC via a GPIB.

3. RESULTS AND DISCUSSION

Characterization of Nanoparticles. We have determined the content of copper in copper-diffused $AgInS_2$ ($AgInS_2$@Cu) by atomic absorption spectroscopy (AAS). Results obtained from different materials have been listed in Table 1. Molar

Table 1. Content of Silver, Indium, and Copper in Copper-Diffused $AgInS_2$ Nanoparticles As Obtained from Atomic Absorption Spectroscopy[a]

amount of injected 0.2 M copper stock solution (mL)	molar % of copper with respect to the total cationic elements in the reaction bath	obtained molar % of Ag	obtained molar % of In	obtained molar % of Cu	molar % of Cu with respect to the total cationic elements in $Cu@AgInS_2$
0	0	22.5	23.4	0	0
0.05	5	21.2	22.1	1.8	4.1
0.10	10	20.3	22.1	3.5	7.7
0.15	15	20.1	21.4	4.4	9.5
0.20	20	17.8	20.3	5.9	13.5

[a]Content of diffused copper was varied by the amount of injected copper salt in the reaction bath (1st column).

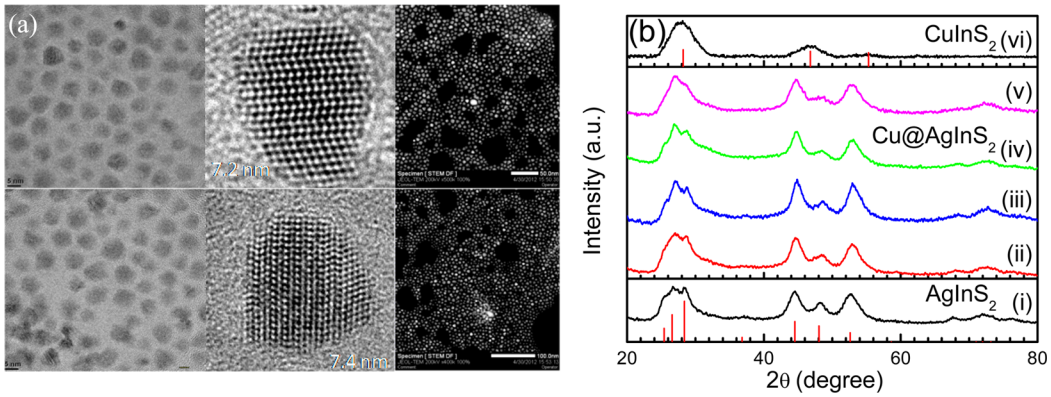

Figure 1. (a) TEM, HR-TEM, and STEM images, respectively, of $AgInS_2$ nanoparticles (upper panel) and $AgInS_2$@Cu(0.10) nanoparticles (lower panel). While the scale bar for the TEM images was 5 nm, the diameters of the nanocrystals obtained from HR-TEM images were 7.2 and 7.4 nm, respectively. (b) XRD spectra of (i) $AgInS_2$ nanoparticles, (ii)−(v) copper-diffused $AgInS_2$ nanoparticles at increasing level of copper diffusion, and (vi) $CuInS_2$ nanoparticles. Diffraction peaks of $AgInS_2$ and $CuInS_2$, as obtained from JCPDS files #25-1328 and #38-0777, respectively, are shown as sticks in the respective ordinates.

weight % of Ag in $AgInS_2$ was slightly lower than the expected value implying possible vacancies at silver sites. In copper-diffused $AgInS_2$, with the content of copper being specified as the weight percent of total cationic elements, we observe that the content increased as the amount of injected copper stock solution in the reaction bath increased. With copper diffusion, the relative content of silver decreased more than that of indium. This implies that, apart from occupying the vacancies, the copper atoms might have replaced some of the cationic elements; replacement may have occurred primarily at the silver sites as compared to the indium ones for all the nanoparticles. If we compare the molar % of copper added to the bath and the molar % of diffused copper with respect to total cationic elements, we find that the latter parameter increased monotonically with the volume of copper solution added during the reaction process. The values moreover did not differ by a large extent; we hence would continue to quote the volume of the copper stock solution added in the bath as a measure of diffused copper in $AgInS_2$ nanoparticles.

Diffusion of copper in $ZnIn_2S_4$ is known to introduce a new state above the valence band (leading to a decrease in band gap) through an interaction between its 3d-state and the valence band-edge of the host nanocrystal.[29] The ratio between silver and indium contents in $AgInS_2$ is also known to have a control over band-positions of the nanoparticles.[30] Here, with a control over copper content in copper-diffused $AgInS_2$, we expect to tune the band gap of the nanoparticles to the low-energy region.

To characterize the nanoparticles, we have recorded their transmission electron microscopy (TEM) images. Figure 1a shows the TEM image of the $AgInS_2$ nanoparticles. The size of the particles was uniform and mostly spherical. A high-resolution TEM (HR-TEM) image of a typical particle, as presented in the same figure, shows that the diameter of the nanoparticles was about 7.2 nm. The HR-TEM image further shows that, though the nanoparticle was largely single crystalline in nature, there were traces of crystalline defects or voids. The dark-field scanning transmission electron microscopy (STEM) image, as shown in Figure 1a, confirms uniform size distribution of the particles. We have studied TEM, HR-TEM, and STEM images of copper-diffused $AgInS_2$ nanoparticles also. A set of images for $AgInS_2$@Cu(0.10) nanoparticles was shown in the lower panel of Figure 1a. From the TEM images, it is clear that copper diffusion in the $AgInS_2$ nanoparticles did neither modulate the shape nor alter the diameter, since the reaction condition remained the same except allowing diffusion of copper to vacant sites of the host nanocrystal. The HR-TEM image here shows that the crystalline defects or voids became absent supporting copper diffusion in the nanoparticles.

For further insights on copper diffusion in $AgInS_2$ nanoparticles, we recorded their X-ray diffraction (XRD) patterns at different levels of copper diffusion. Figure 1b clubs such spectra for different copper-diffused $AgInS_2$ nanoparticles along with that of $CuInS_2$ nanoparticles that were grown separately. The diffraction peaks of $AgInS_2$ nanoparticles readily matched that of the orthorhombic phase of the pure $AgInS_2$ (JCPDS file #25-1328). The peaks for other copper-diffused nanoparticles were quietly matched with that of $AgInS_2$ nanoparticles. A careful analysis of the XRD spectra shows a small but systematic shift of the peaks corresponding to $AgInS_2$ crystals toward the higher angle. The shift, amounting to about 1° when the content of

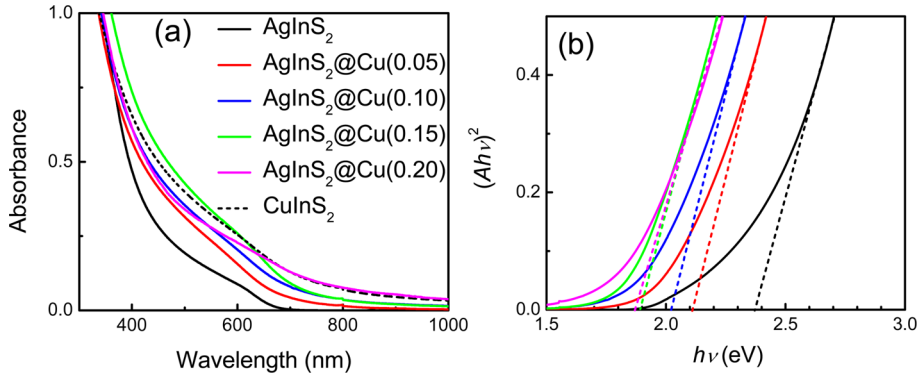

Figure 2. (a) Optical absorption of $CuInS_2$ and copper-diffused $AgInS_2$ nanoparticles in dispersed solution. The contents of diffused copper in $AgInS_2$ nanoparticles are shown in the legend. (b) Plots of $(Ahν)^2$ versus energy. Broken lines have been drawn to determine the intercepts of the linear portion of each plot with the energy axis.

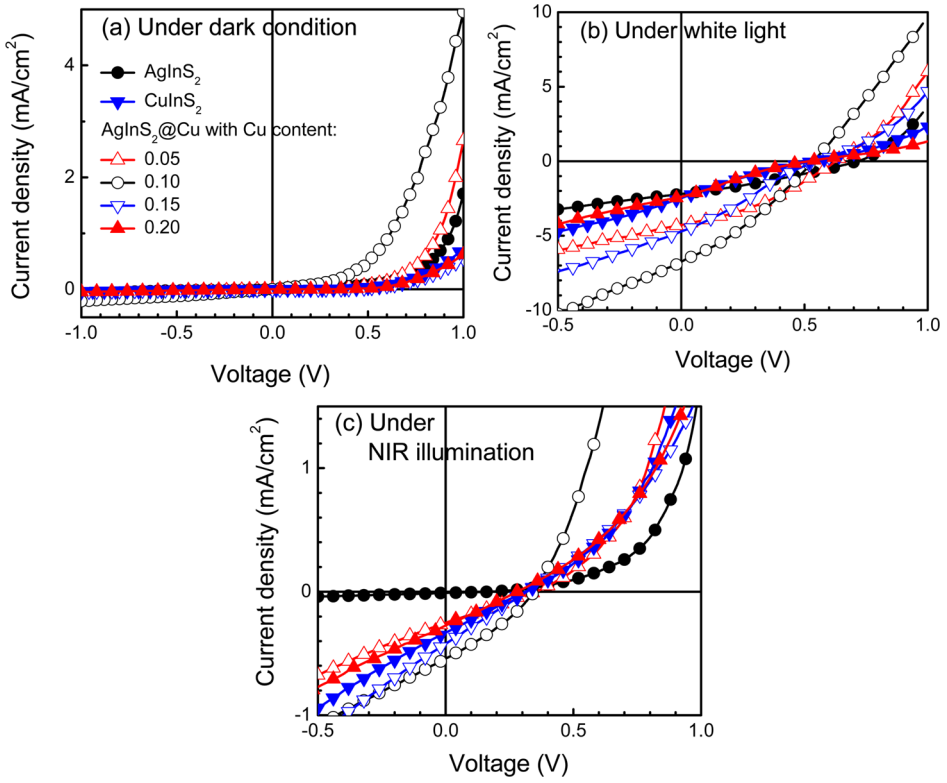

Figure 3. Current–voltage characteristics of copper-diffused $AgInS_2$ nanoparticles and P3HT bulk-heterojunction devices (a) under a dark condition, (b) with white light illumination, and (c) under a near-IR illumination above 650 nm. Contents of the diffused copper in the nanoparticles are shown in the legend. In each of the plots, characteristics of devices based on P3HT:$AgInS_2$ and P3HT:$CuInS_2$ bulk-heterojunction layers are also shown.

diffused copper was the highest, would occur if silver or indium ions were replaced by smaller copper ions. There may be a little bit of difference in peak intensity and peak clarity in copper-diffused nanoparticles. Such a small difference may appear from case-to-case variation in XRD measurements. There could also be an improvement in crystallinity of the particles, since the diffused copper atoms might have removed vacancies and defects from the host materials. To rule out formation of $CuInS_2$ nanoparticles, we compared XRD spectra of copper-diffused $AgInS_2$ nanoparticles and that of $CuInS_2$ nanoparticles grown separately. The spectrum of $CuInS_2$ nanoparticles along with diffraction peaks of the nanoparticles, as shown in Figure 1b(vi), readily matched that of the tetragonal phase of the pure $CuInS_2$ (JCPDS file #38-0777). The diffraction peaks of $CuInS_2$ nanoparticles are generally broad primarily due to crystalline defects and also wide distribution of diameter of the nanoparticles.[31] The peak positions of $CuInS_2$ and $AgInS_2$@Cu nanocrystals did not match at all. In the XRD spectra of $AgInS_2$@Cu nanocrystals, we did not observe diffraction peaks corresponding to copper sulfides or oxides. The results ruled out formation of such compounds and also $CuInS_2$ upon copper diffusion in $AgInS_2$. Hence, we can infer that copper inoculation during the synthesis process did not produce other phases with excess copper remaining unreacted. The copper diffusion in the nanocrystals was further supported by X-ray photoelectron spectroscopy (XPS) that showed the presence of Ag(1), In(III), S(II), and Cu(I) states that supports formation

of the $AgInS_2$ compound (Figure S1 in the Supporting Information).

Optical Characterization of the Nanoparticles. Optical absorption spectra of extracted nanoparticles in chloroform solution are shown in Figure 2a. Onset of absorption for $AgInS_2$ nanoparticles starts from around 670 nm. With copper diffusion within the nanoparticles, the onset shifts toward the red and reaches as high as 850 nm. The results are similar to the reports of red-shift in the spectra upon copper doping in $ZnIn_2S_4$ and ZnO nanoparticles.[29,32] The change in absorption onset may appear due to an interaction between the 3d-state of copper and valence band-edge of the host material.

To visualize the red-shift in a quantitative manner, we have estimated the optical band gap (E_g) of the nanoparticles using the following equation:[33]

$$(\alpha h\nu)^2 = a(h\nu - E_g)$$

where α is the extinction coefficient of nanoparticles and a is a constant. The equation is applicable here due to the fact that $AgInS_2$ is a direct band gap material. If we replace α by A/bc, where A is the total absorption and bc is the product of optical path length and concentration, both of which remained invariant for all the measurements, we can rewrite the equation as:

$$(Ah\nu)^2 = a(h\nu - E_g)$$

with a being another constant. Plots of $(Ah\nu)^2$ versus $h\nu$ are shown in Figure 2b. From the intercept of linear portion of the plot, optical band gap can be estimated if the constant a is known. The plot however clearly shows that the optical band gap of $AgInS_2$ nanoparticles decreases with increasingly more copper diffusion in the nanoparticles.

Current–Voltage Characteristics: Different Nanoparticles in P3HT Matrix. We have recorded I–V characteristics of P3HT:$AgInS_2$@Cu bulk-heterojunction devices under dark and different illumination conditions. Concentration of diffused copper in $AgInS_2$ nanoparticles has been varied for four different values. In addition, devices based on $AgInS_2$ and $CuInS_2$ separately in P3HT matrix have also been characterized. That is, for this set of experiments, we have characterized six different devices. Concentration ratio between P3HT and nanoparticles in all the devices was kept at 1:1. For each of the six device structures, at least five cells were characterized that provided reproducible characteristics.

I–Vs under the dark for all the devices were rectifying in nature. Figure 3a shows such characteristics from the six different devices. Rectification ratio in these bulk-heterojunction devices ranged between 12 and 24 when measured at 1.0 V. Conductivity of $AgInS_2$ with lightly diffused copper in the nanoparticles was higher as compared to that of $AgInS_2$, $CuInS_2$, or $AgInS_2$ nanoparticles having a large concentration of diffused copper.

Rectifying nature of I–V characteristics under the dark condition provides a signature that the devices may act as solar cells under an illumination condition. Characteristics of the devices under 100 mW/cm^2 white light illumination are shown in Figure 3b. While all the devices acted as solar cells, the short-circuit current (I_{SC}) increased with copper diffusion in the nanoparticles. The I_{SC} however decreased afterward, that is, when copper diffusion exceeded an optimum value, Cu(0.10). While I_{SC} reached a value of 6.74 mA/cm^2, the power conversion efficiency of the device was 1.13%. The efficiency would have been higher if the devices returned a higher fill-factor. Open-circuit voltage (V_{OC}) remained in the 0.52–0.72 V range; there has been no particular relationship between V_{OC} and the content of copper diffusion that came across from the measurements. Parameters of the photovoltaic devices have been enlisted in Table 2. We may add here that we fabricated all the devices for at least five times and the quoted parameters were representative values.

Table 2. Parameters of Photovoltaic Devices Based on Different Nanoparticles in P3HT Matrix with a 1:1 Weight Ratio

nanoparticles forming bulk-heterojunction with P3HT	I_{SC} (mA/cm^2)	V_{OC} (V)	fill-factor (%)	power conversion efficiency (%)
$AgInS_2$	2.20	0.72	29.7	0.47
$AgInS_2$@Cu(0.05)	4.27	0.62	35.5	0.94
$AgInS_2$@Cu(0.10)	6.74	0.54	31.0	1.13
$AgInS_2$@Cu(0.15)	4.70	0.56	25.8	0.68
$AgInS_2$@Cu(0.20)	2.38	0.52	21.8	0.27
$CuInS_2$	2.48	0.54	20.9	0.28

Importance of copper diffusion in $AgInS_2$ nanoparticles and consequently use of such nanoparticles in photovoltaic devices can be visualized if near-IR illumination is used to study photovoltaic properties. In Figure 3c, we show I–V characteristics under an illumination above 650 nm, exhibiting near-IR active photovoltaic devices with P3HT:$AgInS_2$@Cu nanoparticle bulk heterojunctions. The plot further shows that the device with P3HT:$AgInS_2$ bulk heterojunction, that is, the device based on nanoparticles without any copper diffusion, did not show any photovoltaic activities under the near-IR illumination. Near-IR activity of P3HT:$AgInS_2$@Cu based devices appeared due to a red-shift of the optical absorption spectra upon copper diffusion in the $AgInS_2$ nanoparticles. For the $CuInS_2$ based devices, though the optical absorption extended until the long wavelength region, the device performance was not impressive. This could be due to the p-type nature of the $CuInS_2$ nanoparticles[20] that may not be favorable in dissociating excitons and carrier transport when placed in the p-type P3HT matrix.

The fill-factor (FF) in the photovoltaic devices based on nanocrystals with a high copper content becomes low. This could be due to an imbalance in carrier transport caused by a lower conductivity of electrons through the nanocrystals. If we concentrate on V_{OC} of the devices and compare their values obtained under white light and under near-IR illumination, we find that the V_{OC} of any particular device was low in the latter illumination case. In a photovoltaic device, two energy offsets, namely, (1) between the LUMO of the polymer and the conduction band (CB) of nanoparticles and (2) the HOMO of the polymer and the valence band (VB) of nanoparticles can dissociate excitons through a charge-transfer process.[34] While excitons generated in P3HT are dissociated by giving away its electrons to the CB of nanoparticles and the holes being transported through the P3HT polymer itself, the excitons generated in the nanoparticles are dissociated by giving their holes to the polymer. Under a white light illumination, the excitons are generated in both P3HT polymer and the nanoparticles. Hence, the offset between the LUMO of polymer and the CB of nanoparticles is the driving force to dissociate excitons photogenerated in P3HT; the other offset is

effective in dissociating excitons generated in $AgInS_2$@Cu nanoparticles. The V_{OC}, on the other hand, is known to depend on the difference between the quasi Fermi levels of electrons and holes in the devices under an illumination condition.[4,34,35]

In the present case, with excitons photogenerating in both the components under white light illumination, a large number of carriers are formed. Under near-IR illumination, on the other hand, the excitons are generated only in $AgInS_2$@Cu nanoparticles. A decrease in V_{OC} under near-IR illumination is hence due to the fact that with fewer carriers in the device the quasi Fermi energy levels do not shift to a large extent. The difference between the Fermi levels or "effective bandgap" of the heterojunction hence becomes low. The V_{OC}, which depends on the difference between the Fermi levels, hence becomes low under near-IR illumination. This is supported by the observation that V_{OC} (and also I_{SC}) decreases with a decrease in light intensity (Figure S2 in the Supporting Information). The analysis has been schematically represented in Figure 4.

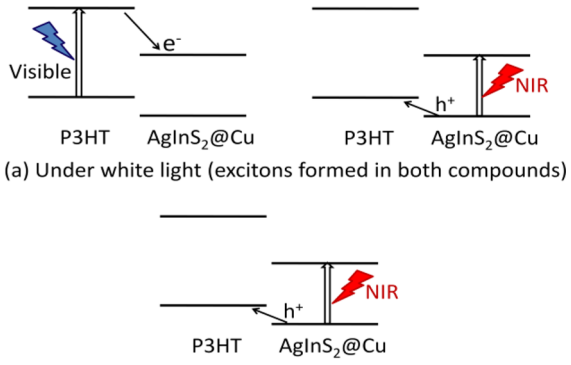

Figure 4. Schematic representation of energy levels of P3HT and band positions of $AgInS_2$@Cu nanoparticles showing the energy-offsets responsible for exciton dissociation under (a) white light and (b) near-IR light illumination.

Impedance Characteristics. It appears that, apart from broadening of optical absorption, the increased conductivity of copper diffused $AgInS_2$ nanoparticles, as observed in $I-V$ characteristics under dark condition, has a role in the improvement in I_{SC} under a white or near-IR light illumination. To substantiate such a possibility, we have recorded impedance spectroscopy of the devices in the 1 Hz to 12 MHz region under a dark condition. No dc bias was applied during the measurements. The Nyquist plots of the devices, plots between real and imaginary components of complex impedance, are presented in Figure 5a. All the plots are semicircular in nature suggesting that the devices could be modeled as a combination of a resistor and a capacitor in parallel. The diameter of the semicircles with the abscissa represents bulk resistance of the devices. The plots show that the bulk resistance indeed decreased when copper-diffused nanoparticles were incorporated in bulk-heterojunction devices.

From the Nyquist plots, one can calculate recombination resistance and chemical capacitance from the low frequency arc of the plots.[36] From the plots presented in Figure 5a, we observe that the diameter of the low frequency arc decreases when copper-diffused nanoparticles were incorporated in the bulk-heterojunction layers. By fitting the semicircular characteristics, we have determined the recombination resistance (R_P), chemical capacitance (C_P), and series resistance (R_S) of different devices (Table 3). Here, the recombination resistor

Table 3. Estimation of Recombination Resistance, Chemical Capacitance, and Parameters of Photovoltaic Devices Based on Different Nanoparticles in P3HT Matrix with a 1:1 Weight Ratio

nanoparticles forming bulk-heterojunction with P3HT	characteristic frequency (Hz)	series resistance (R_S) (Ω)	recombination resistance (R_P) (KΩ)	chemical capacitance (C_S) (nF)
$AgInS_2$	6.7	8.3	537.4	43.9
$AgInS_2$@ Cu(0.05)	12.0	15.3	184.8	71.8
$AgInS_2$@ Cu(0.10)	16.0	6.8	81.6	122.0
$AgInS_2$@ Cu(0.15)	9.0	12.9	277.4	63.8
AgInS2@ Cu(0.20)	5.1	8.8	438.1	71.9
$CuInS_2$	9.0	25.8	551.5	32.1

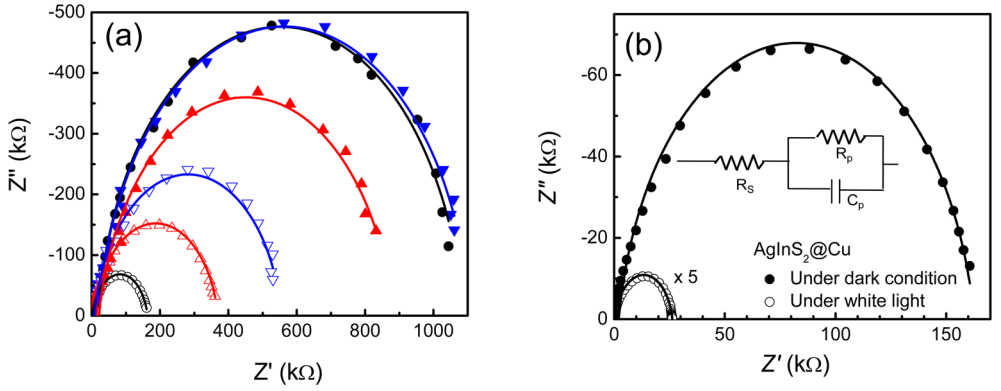

Figure 5. (a) Plots of real and imaginary components of complex impedance of devices based on bulk-heterojunction of P3HT and different nanoparticles under a dark condition. The nanoparticles were $AgInS_2$, $CuInS_2$, and copper diffused $AgInS_2$ having different levels of diffused copper in the nanoparticles. The particles are represented by different symbols, which have the same meaning as in Figure 3a. (b) Similar plots for a device based on bulk-heterojunction of P3HT and $AgInS_2$@Cu(0.10) nanoparticles under dark and white light conditions. The lines in each of the figures are fits to experimental data considering the devices to be an electrical analogue (shown in the inset) with a capacitor (C_P) and a resistor (R_P) in parallel configuration connected to a small series resistor (R_S) in series.

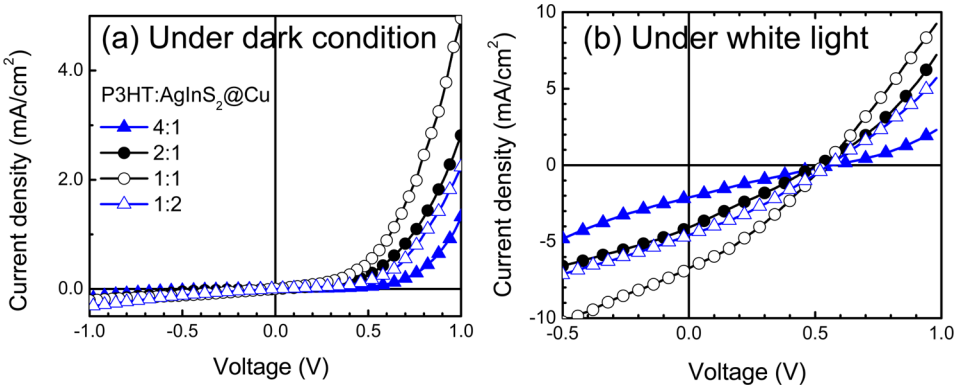

Figure 6. Current–voltage characteristics of P3HT and $AgInS_2$@Cu(0.10) nanoparticles bulk-heterojunction devices (a) under dark condition and (b) with white light illumination. Weight ratios between P3HT and the nanocrystals were varied and are shown in the legend.

and chemical capacitor are connected in a parallel configuration along with R_s in series. From the results presented in Table 3, we find that the recombination resistance of the device based on $AgInS_2$@Cu(0.10) nanoparticles is the least. The results hence support that, with incorporation of $AgInS_2$@Cu(0.10) nanoparticles, the barriers with the electrodes and accordingly the carrier transport became easier leading to increased I_{SC} under the illumination condition. We have recorded impedance characteristics of the devices also under white light. Results for a device under dark and white light are shown in Figure 5b. The diameter of the semicircle shrunk abruptly upon illumination. All the devices returned a similar trend. In the device based on $AgInS_2$@Cu(0.10), the diameter of Nyquist plot decreased from 81.6 to 2.7 kΩ. The sharp decrease in device resistance under illumination may have occurred due to generation of free carriers upon exciton dissociation in the device.

Current–Voltage Characteristics: Varying Concentration between P3HT and $AgInS_2$@Cu Nanoparticles. We have characterized another set of devices, namely, devices where weight ratios between P3HT and the $AgInS_2$@Cu(0.10) nanoparticles were varied as 4:1, 2:1, 1:1, and 1:2. *I–V* characteristics under dark and white light illumination are presented in Figure 6a,b, respectively. The characteristics under the dark are expectedly rectifying in nature. Since current through the devices depends both on the barrier heights for carriers with the electrodes and also on intrinsic conductivity of the active layer, the current at a voltage was optimum for a P3HT:nanoparticle ratio of 1:1. At such a weight ratio, the nanoparticles might have provided suitable hopping pathways without increasing barrier heights for charge carriers. Under white light illumination (100 mW/cm^2), the devices acted as solar cells. Results, as presented in Figure 6b, show that I_{SC} depended on the weight ratio between the components. Power conversion efficiency ranged between 0.28 and 1.13%, with the 1:1 ratio being the optimum. The V_{OC} expectedly did not vary at all, since the materials of the bulk-heterojunction remained the same. That is, since the quasi Fermi energy levels of the polymer and nanostructures under illumination determine V_{OC} of photovoltaic solar cells, the V_{OC} did not vary with the weight ratio between the components. This is in contrast to the results obtained when content of diffused copper in $AgInS_2$ was varied; the content of copper changes the conduction and valence band-edges of the nanoparticles and hence the Fermi energy that determined the V_{OC} of the devices based on such nanoparticles.

I–V characteristics of the devices under exclusively near-IR illumination are shown in Figure 7. The photovoltaic nature has

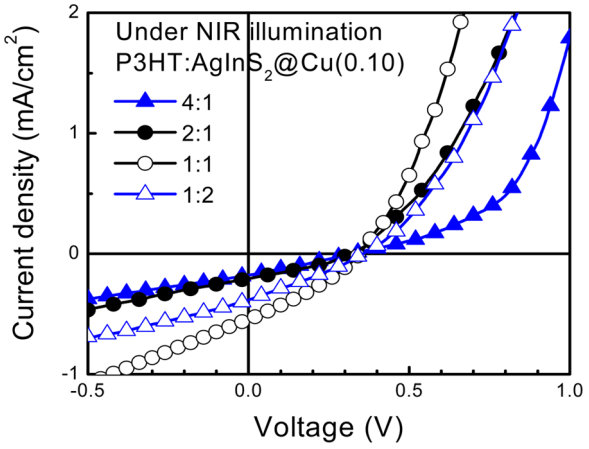

Figure 7. Current–voltage characteristics of P3HT and copper-diffused $AgInS_2$ nanoparticles bulk-heterojunction devices under NIR illumination above 650 nm. Content of diffused copper in the nanoparticles was 10%. Weight ratios between P3HT and $AgInS_2$@Cu were varied and are shown in the legend.

been observed in the characteristics of all the devices. Similar to the characteristics under white light, the V_{OC} under near-IR light did not vary with the ratio between the concentration of P3HT and nanoparticles. Here also, the V_{OC} remained lower than that under white light illumination. As has been explained earlier, the V_{OC} under the near-IR light is low due to fewer number of charge carriers that in turn affects the quasi Fermi energy of the components. It may be recalled that, under white light, a large number of excitons were generated in P3HT and nanoparticles that in turn became dissociated and yielded a large number of carriers. In contrast, under near-IR light, excitons were generated only in the nanoparticles and hence resulted in a fewer number of charge carriers.

External Quantum Efficiency (EQE) Spectra. We have recorded EQE spectra of P3HT:nanoparticle bulk-heterojunction devices. To study the effect of copper diffusion in $AgInS_2$ nanoparticles, we have compared spectra of P3HT:$AgInS_2$ and P3HT:$AgInS_2$@Cu devices (Figure 8). The EQE spectra matched the optical absorption spectrum of P3HT superimposed with a higher-energy continuum due to the nanoparticles. The results show that, with copper diffusion, EQE spectrum extends toward the longer wavelength. With an

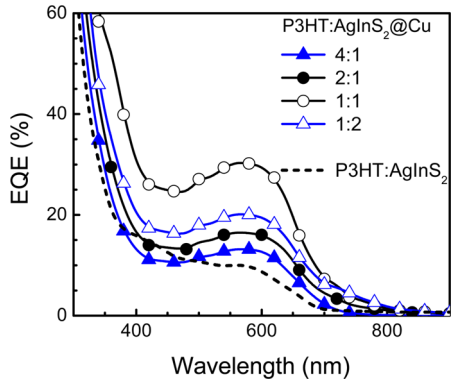

Figure 8. External quantum efficiency spectra of bulk-heterojunction devices based on P3HT and copper-diffused $AgInS_2$ nanoparticles under white light illumination. Content of diffused copper in the nanoparticles was 10%. Weight ratios between P3HT and $AgInS_2$@Cu were varied and are shown in the legend. In addition, the spectrum of a device based on P3HT:$AgInS_2$ bulk-heterojunction layer is shown in the figure.

increase in the weight ratio of copper diffused nanoparticles in P3HT matrix beyond 1:1, the near-IR component of EQE spectrum becomes enhanced; the magnitude at peak wavelength that appears due to the absorption band of P3HT however decreased. The results hence show that the optimum device, having a weight ratio of 1:1 between P3HT and $AgInS_2$@Cu nanoparticles, yields near-IR active bulk-heterojunction hybrid solar cells with also an optimum efficiency in the visible region.

4. CONCLUSIONS

In conclusion, we have grown and characterized copper diffused $AgInS_2$ nanoparticles. Copper diffusion occurs mostly in silver sites and improves the crystallinity of the host $AgInS_2$ nanoparticles. We have introduced such nanoparticles in the P3HT matrix as organic/inorganic bulk-heterojunctions, and the devices based on such nanoparticles acted as photovoltaic solar cells. We have observed that copper diffusion improves short-circuit current of the photovoltaic devices presumably due to broader optical absorption and an increased carrier conduction through the nanocrystals. With an increase in the content of copper diffusion in $AgInS_2$ nanoparticles, the EQE spectrum of bulk-heterojunction devices based on the nanoparticles and P3HT extended toward the longer wavelength making the devices act as near-IR active solar cells. We varied the content of diffused copper in $AgInS_2$ nanoparticles and also the ratio between P3HT and the nanoparticles in bulk-heterojunctions in order to optimize internal resistance of the devices and the hopping conduction process without increasing barrier heights for charge carriers.

■ ASSOCIATED CONTENT

Supporting Information

High-resolution XPS spectra of Ag3d, In3d, S2p, and Cu2p; plots of short-circuit current and open-circuit voltage of $AgInS_2$@Cu(0.10) nanoparticles. This material is available free of charge via the Internet at http://pubs.acs.org.

■ AUTHOR INFORMATION

Corresponding Author

*Tel: +91-33-24734971. Fax: +91-33-24732805. E-mail: sspajp@iacs.res.in.

Notes

The authors declare no competing financial interest.

■ ACKNOWLEDGMENTS

The authors acknowledge financial assistance from DeitY and SERIIUS projects. A.G. and A.J.P. acknowledge CSIR Junior Research Fellowship No. 09/080(0505)/2006-EMR-I (Roll No. 503974) and Ramanna Fellowship SR/S2/RFCMP-01/2009, respectively.

■ REFERENCES

(1) Beek, W. J. E.; Wienk, M. M.; Janssen, R. A. J. *Adv. Mater.* **2004**, *16*, 1009−1013.
(2) Palaniappan, K.; Murphy, J. W.; Khanam, N.; Horvath, J.; Alshareef, H.; Quevedo-Lopez, M.; Biewer, M. C.; Park, S. Y.; Kim, M. J.; Gnade, B. E.; Stefan, M. C. *Macromolecules* **2009**, *42*, 3845−3848.
(3) Martinez-Ferrero, E.; Albero, J.; Palomares, E. *J. Phys. Chem. Lett.* **2010**, *1*, 3039−3045.
(4) Brandenburg, J. E.; Jin, X.; Kruszynska, M.; Ohland, J.; Kolny-Olesiak, J.; Riedel, I.; Borchert, H.; Parisi, J. *J. Appl. Phys.* **2011**, *110*, 064509.
(5) Dayal, S.; Reese, M. O.; Ferguson, A. J.; Ginley, D. S.; Rumbles, G.; Kopidakis, N. *Adv. Funct. Mater.* **2010**, *20*, 2629−2635.
(6) Guchhait, A.; Rath, A. K.; Pal, A. J. *Sol. Energy Mater. Sol. Cells* **2011**, *95*, 651−656.
(7) Kim, K.; Carroll, D. L. *Appl. Phys. Lett.* **2005**, *87*, 203113.
(8) Mattoussi, H.; Rubner, M. F.; Zhou, F.; Kumar, J.; Tripathy, S. K.; Chiang, L. Y. *Appl. Phys. Lett.* **2000**, *77*, 1540−1542.
(9) Pradhan, B.; Batabyal, S. K.; Pal, A. J. *Appl. Phys. Lett.* **2006**, *88*, 093106.
(10) Sun, B. Q.; Greenham, N. C. *Phys. Chem. Chem. Phys.* **2006**, *8*, 3557−3560.
(11) Feng, Y. Y.; Yun, D. Q.; Zhang, X. Q.; Feng, W. *Appl. Phys. Lett.* **2010**, *96*, 093301.
(12) Kashiwaba, Y.; Isojima, K.; Ohta, K. *Sol. Energy Mater. Sol. Cells* **2003**, *75*, 253−259.
(13) Lopez-Luke, T.; Wolcott, A.; Xu, L. P.; Chen, S. W.; Wcn, Z. H.; Li, J. H.; De La Rosa, E.; Zhang, J. Z. *J. Phys. Chem. C* **2008**, *112*, 1282−1292.
(14) Santra, P. K.; Kamat, P. V. *J. Am. Chem. Soc.* **2012**, *134*, 2508−2511.
(15) Shalom, M.; Albero, J.; Tachan, Z.; Martinez-Ferrero, E.; Zaban, A.; Palomares, E. *J. Phys. Chem. Lett.* **2010**, *1*, 1134−1138.
(16) Chang, J. Y.; Su, L. F.; Li, C. H.; Chang, C. C.; Lin, J. M. *Chem. Commun.* **2012**, *48*, 4848−4850.
(17) Li, T. L.; Lee, Y. L.; Teng, H. *Energy Environ. Sci.* **2012**, *5*, 5315−5324.
(18) Sasamura, T.; Okazaki, K.; Kudo, A.; Kuwabata, S.; Torimoto, T. *RSC Adv.* **2012**, *2*, 552−559.
(19) Kuo, K. T.; Liu, D. M.; Chen, S. Y.; Lin, C. C. *J. Mater. Chem.* **2009**, *19*, 6780−6788.
(20) Cho, J. W.; Park, S. J.; Kim, J.; Kim, W.; Park, H. K.; Do, Y. R.; Min, B. K. *ACS Appl. Mater. Interfaces* **2012**, *4*, 849−853.
(21) Maier, E.; Rath, T.; Haas, W.; Werzer, O.; Saf, R.; Hofer, F.; Meissner, D.; Volobujeva, O.; Bereznev, S.; Mellikov, E.; Amenitsch, H.; Resel, R.; Trimmel, G. *Sol. Energy Mater. Sol. Cells* **2011**, *95*, 1354−1361.
(22) Nam, M.; Lee, S.; Park, J.; Kim, S. W.; Lee, K. K. *Jpn. J. Appl. Phys.* **2011**, *50*, 06GF02.
(23) Krustok, J.; Raudoja, J.; Krunks, M.; Mandar, H.; Collan, H. *J. Appl. Phys.* **2000**, *88*, 205−209.
(24) You, S. H.; Hong, K. J.; Youn, C. J.; Jeong, T. S.; Moon, J. D.; Kim, H. S.; Park, J. S. *J. Appl. Phys.* **2001**, *90*, 3894−3898.
(25) Ikeda, S.; Nakamura, T.; Harada, T.; Matsumura, M. *Phys. Chem. Chem. Phys.* **2010**, *12*, 13943−13949.
(26) Tsuji, I.; Shimodaira, Y.; Kato, H.; Kobayashi, H.; Kudo, A. *Chem. Mater.* **2010**, *22*, 1402−1409.

(27) Tang, X. S.; Yu, K. A.; Xu, Q. H.; Choo, E. S. G.; Goh, G. K. L.; Xue, J. M. *J. Mater. Chem.* **2011**, *21*, 11239−11243.
(28) Tang, X. S.; Ho, W. B. A.; Xue, J. M. *J. Phys. Chem. C* **2012**, *116*, 9769−9773.
(29) Shen, S. H.; Zhao, L.; Zhou, Z. H.; Guo, L. J. *J. Phys. Chem. C* **2008**, *112*, 16148−16155.
(30) Cheng, K. W.; Liu, P. H. *Sol. Energy Mater. Sol. Cells* **2011**, *95*, 1859−1866.
(31) Li, T. L.; Teng, H. S. *J. Mater. Chem.* **2010**, *20*, 3656−3664.
(32) Elilarassi, R.; Chandrasekaran, G. *J. Mater. Sci.: Mater. Electron.* **2010**, *21*, 1168−1173.
(33) Woo, K.; Kim, Y.; Moon, J. *Energy Environ. Sci.* **2012**, *5*, 5340−5345.
(34) Deibel, C.; Strobel, T.; Dyakonov, V. *Adv. Mater.* **2010**, *22*, 4097−4111.
(35) Scharber, M. C.; Wuhlbacher, D.; Koppe, M.; Denk, P.; Waldauf, C.; Heeger, A. J.; Brabec, C. L. *Adv. Mater.* **2006**, *18*, 789−794.
(36) Fabregat-Santiago, F.; Garcia-Belmonte, G.; Mora-Sero, I.; Bisquert, J. *Phys. Chem. Chem. Phys.* **2011**, *13*, 9083−9118.